HHS Public Access

Author manuscript

J Am Chem Soc. Author manuscript; available in PMC 2021 March 30.

Published in final edited form as:

J Am Chem Soc. 2020 January 29; 142(4): 1925–1932. doi:10.1021/jacs.9b11207.

Cyclodextrin-Based Peptide Self-Assemblies (Spds) That Enhance Peptide-Based Fluorescence Imaging and Antimicrobial Efficacy

Jin-Biao Jiao[∇],
East China University of Science and Technology, Shanghai, P. R. China, and Université Paris-Saclay, ENS Paris-Saclay, CNRS, PPSM, Cachan, France

Guan-Zhen Wang[∇],
Chinese Academy of Sciences, Shanghai, P. R. China, and University of Chinese Academy of Sciences, Beijing, P. R. China

Xi-Le Hu[∇],
East China University of Science and Technology, Shanghai, P. R. China

Yi Zang,
Chinese Academy of Sciences, Shanghai, P. R. China

Stéphane Maisonneuve,
Université Paris-Saclay, ENS Paris-Saclay, CNRS, PPSM, Cachan, France

Adam C. Sedgwick,
The University of Texas at Austin, Austin, Texas

Jonathan L. Sessler[*],
The University of Texas at Austin, Austin, Texas

Juan Xie[*],
Université Paris-Saclay, ENS Paris-Saclay, CNRS, PPSM, Cachan, France

Jia Li[*],
Chinese Academy of Sciences, Shanghai, P. R. China, University of Chinese Academy of Sciences, Beijing, P. R. China, and Open Studio for Druggability Research of Marine Natural Products Pilot National Laboratory for Marine Science and Technology (Qingdao), Aoshanwei, P. R. China

[*]Corresponding Authors **Jonathan L. Sessler** – The University of Texas at Austin, Austin, Texas; Sessler@cm.utexas.edu, **Juan Xie** – Université Paris-Saclay, ENS Paris-Saclay, CNRS, PPSM, Cachan, France; joanne.xie@ens-cachan.fr, **Jia Li** – Chinese Academy of Sciences, Shanghai, P. R. China, University of Chinese Academy of Sciences, Beijing, P. R. China, and Open Studio for Druggability Research of Marine Natural Products Pilot National Laboratory for Marine Science and Technology (Qingdao), Aoshanwei, P. R. China; jli@simm.ac.cn, **Xiao-Peng He** – East China University of Science and Technology, Shanghai, P. R. China; xphe@ecust.edu.cn.

[∇]These authors contributed equally.

Complete contact information is available at: https://pubs.acs.org/10.1021/jacs.9b11207

ASSOCIATED CONTENT

Supporting Information

The Supporting Information is available free of charge at https://pubs.acs.org/doi/10.1021/jacs.9b11207.

Additional schemes and figures, experimental section, and copies of original spectra (PDF)

The authors declare no competing financial interest.

Xiao-Peng He*,
East China University of Science and Technology, Shanghai, P. R. China

He Tian
East China University of Science and Technology, Shanghai, P. R. China

Abstract

As a result of their high specificity for their corresponding biological targets, peptides have shown significant potential in a range of diagnostic and therapeutic applications. However, their widespread use has been limited by their minimal cell permeability and stability in biological milieus. We describe here a hepta-dicyanomethylene-4*H*-pyran appended β-cyclodextrin (**DCM$_7$-β-CD**) that acts as a delivery enhancing "host" for 1-bromonaphthalene-modified peptides, as demonstrated with peptide probes **P1–P4**. Interaction between the fluorescent peptides **P1–P3** and **DCM$_7$-β-CD** results in the hierarchical formation of unique supramolecular architectures, which we term supramolecular-peptide-dots (**Spds**). Each **Spd** (**Spd-1**, **Spd-2**, and **Spd-3**) was found to facilitate the intracellular delivery of the constituent fluorescent probes (**P1–P3**), thus allowing spatiotemporal imaging of an apoptosis biomarker (caspase-3) and mitosis. **Spd-4**, incorporating the antimicrobial peptide **P4**, was found to provide an enhanced therapeutic benefit against both Gram-positive and Gram-negative bacteria relative to **P4** alone. In addition, a fluorescent **Spd-4** was prepared, which revealed greater bacterial cellular uptake compared to the peptide alone (**P4-FITC**) in *E. coli*. (ATCC 25922) and *S. aureus* (ATCC 25923). This latter observation supports the suggestion that the **Spd** platform reported here has the ability to facilitate the delivery of a therapeutic peptide and provides an easy-to-implement strategy for enhancing the antimicrobial efficacy of known therapeutic peptides. The present findings thus serve to highlight a new and effective supramolecular delivery approach that is potentially generalizable to overcome limitations associated with functional peptides.

Graphical Abstract

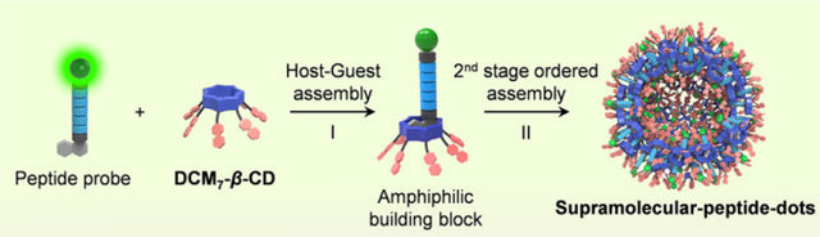

INTRODUCTION

Biological peptides are naturally occurring compounds that are responsible for a number of physiological processes, including cell growth and development, cell metabolism, signal transmission, immunoregulation, and reproduction.[1–3] Taking advantage of their high specificity toward their corresponding biological receptors, researchers have exploited both natural and synthetic peptides in chemical biology and therapy.[4–7] To date, peptides have been developed into antibiotics, vaccines, and therapeutic agents that often provide for improved efficacy with minimal side effects and toxicity.[8,9] Additionally, efforts have been

made to develop peptide-based imaging agents for use in conjunction with a number of common modalities, including MRI, PET/SPECT, and luminescence.[10–12] Unfortunately, the widespread use of functional peptides has been limited because they are generally hydrophilic, charged, and structurally complex. This compromises their ability to cross the hydrophobic cell membrane to deliver a therapeutic payload or to produce the desired spatiotemporal image of a specific biological target or biomarker.

To address these issues, cell-permeable entities have been attached directly to peptides in the attempt to enhance cellular uptake.[13,14] This includes the use of the cell-penetrating peptides, such as TAT (derived from the trans-activating transcriptional activator (Tat) from HIV-1) and penetratin. However, these strategies can alter the biological activity of the peptide or trigger unwanted enzymatic degradation prior to reaching the desired location in vivo.[15] Metallic nanoparticles[16] and low-dimensional materials, such as graphene oxide and graphene-like constructs,[17] have also been used to promote the clustering of peptide probes and to increase their intracellular accumulation. These elegant strategies have inspired the study of other organic functional materials that can promote peptide self-assembly and potentiate cell permeability.[18] However, systems that permit morphological control over supramolecular-based nanoparticles and permit effective delivery of active peptides remain limited in number. This reflects, in part, the finding that simple changes in size, shape, and surface charge can have a significant impact on the cell internalization, substrate (e.g., drug or fluorophore) release, and in vivo physiochemical properties of the nanoparticle.[19]

Cyclodextrins (CDs) are highly biocompatible cyclic macromolecules that have found use in a range of biomedical applications, including drug delivery, biosensing/bioimaging, and formation of functional supramolecular-ensembles of therapeutic value.[20–26] We recently reported the modification of the narrow rim of β-CD with pyrene via a so-called “click” reaction. This functionalization facilitated its interaction with a rhodamine-based fluorescent glycoprobe and afforded a self-assembled fluorogenic probe capable of detecting lectins selectively in homogeneous buffer solution.[27]

As detailed below, we have now created a hepta-dicyanomethylene-4*H*-pyran-appended β-cyclodextrin derivative, **DCM$_7$-β-CD**. This modified cyclodextrin acts as an effective host for 1-bromonaphthalene-modified peptides, including the FITC-tagged fluorescent probes **P1–P3** and the antimicrobial probe **P4** (all of which function as β-CD guests; Figure 1). The interaction between the FITC-bearing peptides **P1–P3** and **DCM$_7$-β-CD** results in the formation of **DCM$_7$-β-CD**/P supramolecular-ensembles that undergo further ordered self-assembly to afford unique architectures, which we have termed supramolecular-peptide-dots, **Spds** (Figure 2). The present **Spds** were found to provide enhanced cell permeability compared to the starting peptides alone and, in the case of **P1–P3**, allow for the imaging of the apoptosis biomarker, caspase-3 (cysteinyl aspartate specific proteinase-3), in Hep-G2 cells (Figure 2) and the monitoring of cell mitosis in HeLa cells. The **Spd** based on **P4** (**Spd-4**) was shown to provide an increase in therapeutic efficacy toward both Gram-positive and Gram-negative bacteria relative to **P4** alone. Taken in concert, the present results provide support for the notion that the **Spd** approach could provide a convenient and effective means of enhancing the therapeutic and imaging potential of peptides that otherwise display limited cell permeability and bioactivity.

DCM_7-β-CD was synthesized through the coupling of seven propargyl-functionalized dicyanomethylene-4*H*-pyran (DCM) subunits to an azido-functionalized β-CD under traditional "click" reaction conditions ($CuSO_4$ and sodium ascorbate). This provided the desired cyclodextrin host in 78% yield (Figure 1 and Scheme S1).[28,29] The fluorescent peptide-based probes (**P1–P3**) were synthesized by solid-phase methods and yielded peptides bearing 1-bromonaphthalene and FITC substituents on the *N*- and *C*-termini, respectively (Figure 1 and Scheme S1). Probes **P1** and **P2** contain the sequences 3 Pal-D-βhLeu-F-D (for **P1**) and DEVD (for **P2**), respectively. These are known substrates for caspase, a well-established biomarker to track cell apoptosis.[30] In contrast, probe **P3** contains the sequence VARVGSPPD, which is known to bind to tubulin, a structural protein that is essential for cell mitosis.[31] The antimicrobial peptide (AVDRAV) was modified with 1-bromonaphthalene to afford **P4** (Figure 1).

Primarily, probes **P1**, **P2**, and **P3** and **DCM_7-β-CD** were used to explore the ability of the **DCM_7-β-CD** host to stabilize self-assembled supramolecular structures when exposed to these peptide guests. The addition of both host and a guest to a phosphate buffered saline solution (0.1 M, pH 7.4), followed by sonication for 30 min, resulted in the formation of the corresponding supramolecular-peptide-dots, **Spd-1**, **Spd-2**, and **Spd-3**. Each **Spd** was characterized by high-resolution transmission electron microscopy (HRTEM), dynamic light scattering (DLS), and optical spectroscopy. HRTEM imaging (Figure 3a) revealed structurally unique morphologies that were dependent upon the specific peptide used. In particular, "donut-like" hollow structures were observed for **Spd-1** and **Spd-2**, whereas the formation of solid particles was seen in the case of **Spd-3**. DLS was then used to determine the particle size of each **Spd** and the free host (Figure 3b). The diameter of **DCM_7-β-CD** alone was found to be approximately 1100 nm; this is a value consistent with the formation of aggregated species in aqueous solution. In contrast, the diameter of each **Spd** was found to be considerably smaller (around 100 nm), as would be expected for ordered complexes.

Further support for the formation of the proposed **Spds** came from fluorescence quenching studies. When probes **P1–P3** are bound to **DCM_7-β-CD**, the FITC fluorescence emission is suppressed as the result of Förster resonance energy transfer (FRET). FRET quenching was expected based on UV–vis spectroscopic experiments that confirmed significant spectral overlap between the emission and absorption bands of the FITC fluorophore on the probes and the DCM fluorophores on the **DCM_7-β-CD** host (Figure S1).[32–34] In accord with these expectations, detailed fluorescence titrations, involving the addition of **DCM_7-β-CD** to each peptide probe (**P1–P3**), led to a concentration-dependent fluorescence quenching of the FITC emission (Figure 4a,d,g). Notably, a slight increase in the DCM fluorescence intensity was also observed. These findings are consistent with FRET and the formation of the proposed **Spds**. No significant change in the fluorescent intensity was observed across a wide pH range (3–12) for each **Spd** (Figure S2). This finding was considered as auguring well for their use in biological applications.

We next evaluated the response of **Spd-1** and **Spd-2** when exposed to the enzyme caspase-3. As shown in Figure 4b/e, the addition of caspase-3 to both **Spd-1**/**Spd-2** resulted in a significant increase in the FITC-derived fluorescence emission intensity. This was taken as

evidence that **P1**/**P2** undergo enzymatic cleavage, a process that disrupts the FRET through the release of free FITC. Further confirming this, TEM imaging and DLS analysis for **Spd-1**, in the presence of caspase-3, revealed a change in morphology which looked similar to that of **DCM$_7$-β-CD** (Figure S3).

In the case of **Spd-3**, the effect of the structural protein tubulin was tested. As can be seen from an inspection of Figure 4h, a restoration in fluorescence emission intensity was also observed. In this case, however, disassembly of **Spd-3** and disruption of the FRET process was considered to be the result of probe **P3** binding to tubulin.

As a predicate to testing **Spd-1**, **Spd-2**, and **Spd-3** in cellular imaging, selectivity studies involving a range of different enzyme/proteins were performed. As shown in Figure 4c,f, **Spd-1** and **Spd-2** proved selective for caspase-type enzymes (e.g., caspase-3 and caspase-7). However, **Spd-1** was shown to be selective solely for caspase-3 whereas **Spd-2** proved to be a substrate for both caspase-3 and caspase-7.[35] **Spd-3** demonstrated a remarkable selectivity for tubulin as compared to other physiologically relevant proteins (Figure 4i). The excellent selectivity observed for the **Spds** is believed to be the result of their high specificity for their corresponding enzyme/protein, coupled with an additional “protective effect” arising from the **Spd** platform. It further prompted us to evaluate the utility of the present **Spds** in cellular imaging applications. Toward this end, the peptide probes (**P1**, **P2**, and **P3**) and the corresponding **Spd** systems (**Spd-1**, **Spd-2**, and **Spd-3**) were compared.

To test probes **Spd-1** and **Spd-2** in the context of cellular imaging of apoptosis-related biomarkers, Hep-G2 (human hepatoma cell) cells were treated with PA (palmitic acid) to elicit cell apoptosis and activate the caspase enzymes.[36] Initially, Hep-G2 cells were treated with **P1** and **P2**. This led to no appreciable increase in the FITC-derived fluorescence intensity as a function of increasing concentration for both apoptotic and nonapoptotic Hep-G2 cells (Figure 5). In contrast, incubation of **Spd-1** (Figure 5a,b) and **Spd-2** (Figure 5c,d) with the same apoptotic cells [PA(+)] led to a remarkable concentration-dependent fluorescence enhancement. In addition, the fluorescence enhancement of **Spd-1** was shown to be dependent on both the concentration of PA (Figure S4a,b) and the incubation time (Figure S4c,d). These results support the proposal that **Spds** can be used to enhance into-cell internalization of peptide probes, such as **P1** and **P2**. The broad applicability of these supramolecular-based imaging agents was shown through the use of an additional cell line (HeLa) with **Spd-2**. Again, a concentration-dependent fluorescence increase was observed when these cells were preincubated with PA (Figure S5). In addition, **Spd-2** was shown capable of monitoring the drug-induced apoptosis seen upon incubation with the well-known anticancer drug (cisplatin); this proved true in both the Hep-G2 and HeLa cell lines (Figure S6). This finding was taken as support for the notion that the present **Spds** may find use as cell imaging tools.

For the tubulin substrates **P3** and **Spd-3**, the fluorescence imaging properties were evaluated in HeLa cells, a cell line that overexpresses microtubules.[37] Incubation of these cells with **P3** led to a weak fluorescence signal being observed, as would be expected for a peptide with poor cell permeability. In contrast, a concentration-dependent fluorescence enhancement was observed upon incubation with **Spd-3** (the microtubules of the cells were fused with

mCherry for colocalization with the fluorescence of **Spd-3**; Figure 6a,b). As above, this difference is ascribed to the enhanced cell permeability of this **Spd** construct. Using **Spd-3** it proved possible to image the morphological changes in the microtubules during the entire mitotic process of the HeLa cells (Figure 6c). Confirmation of this ability came from experiments wherein **Spd-3** was studied in conjunction with mCherry fused microtubules. Lastly, flow cytometry studies were carried out; they provided support for the proposed cell internalization of each **Spd** in that the number of cells producing a fluorescence signature increased with increasing concentrations of **Spd** (Figures S7–S9).

The development of antibiotic resistant bacteria, a problem exacerbated through the widespread misuse of antibiotics, is rendering inactive antibiotics spanning multiplicity of classes.[38] Recent efforts to generate new antibiotics have focused on peptides as a potentially effective strategy to combat bacterial infections. However, as with other peptide-based agents cell uptake issues remain to be addressed. To test whether the present **Spd** nanoparticle strategy could help overcome these limitations, the known antimicrobial peptide (AVDRAV)[39] was modified with 1-bromonaphthalene to afford **P4** (Figure 1). Self-assembly of **P4** with **DCM$_7$-β-CD** produced **Spd-4**. This proposed self-assembly leads to a decrease in the particle size as inferred from dynamic light scattering (DLS) studies (Figure S10); this is as expected for the formation of an **Spd**.

Spd-4 was evaluated for its putative activity against both Gram-negative [*Escherichia coli* (*E. coli*, ATCC 25922)] and Gram-positive [*Staphylococcus aureus* (*S. aureus* ATCC 25923)] bacteria strains. Using the plate counting method, **Spd-4** demonstrated an enhanced antimicrobial effect compared to **P4** alone (Figure 7a). Cell viability studies involving these two bacterial strains provided further support for this observation (Figure 7b). Although the precise mechanism as to how **Spd-4** improves the bioactivity of the peptide remains to be elaborated, we believe it reflects improved through-membrane transport in analogy to what was observed for **Spds-1–3**.

To test the above hypothesis, an FITC-labeled version **P4** (**P4-FITC**, Figure 1) was synthesized and used to assemble a fluorescent version of **Spd-4**. Fluorescence imaging experiments using *E. coli*. (ATCC 25922) and *S. aureus* (ATCC 25923) revealed a stronger fluorescence signal for **Spd-4** as compared to **P4-FITC** alone in the case of both bacteria (Figure S11). These results provide further support for the contention that the **Spd** strategy reported here allows for the enhanced delivery of an antimicrobial peptide. We do recognize, however, that alternative mechanisms could be envisioned that account for the enhancement produced by **Spd-4**.[40] Nevertheless, in strictly operational terms, these additional results provide direct experimental support for the notion that the present **Spd** strategy may be used to enhance the therapeutic efficacy of an antimicrobial peptide.

To test further the applicability of the **Spd** strategy, two clinically isolated bacteria (*P. aeruginosa* (3887) and *A. baumannii* (AB-1617), of which the latter is a known multidrug resistant strain) were evaluated with **Spd-4**. To our delight, **Spd-4** was shown to have an enhanced inhibitory efficacy against both bacterial strains when compared to **P4** alone (Figure S12); again, this finding provides support for the suggestion that the present supramolecular approach may be used to enhance the efficacy of a therapeutic peptide.

In summary, we have developed a novel DCM-appended *β*-cyclodextrin **DCM$_7$-*β*-CD**. In the presence of 1-bromonaphthalene-modified functional peptides (**P1–P4**), this host undergoes an ordered self-assembly process to afford structurally unique supramolecular architectures, so-called **Spds**. HRTEM images and DLS analyses revealed peptide dependent particle morphologies with diameters of ~100 nm. The **Spds** prepared from probes **P1**-**P3** demonstrated excellent cell permeability, which facilitated the intracellular delivery of the constituent probe and enabled the intracellular cellular imaging of an apoptosis biomarker (caspase-3) and mitosis events. The present self-assembly strategy was extended to include an antimicrobial peptide and was found to improve efficacy in the case of both Gram-positive and –negative bacteria. In addition, a fluorescent **Spd-4** was developed. It engendered greater bacteria cellular uptake relative to peptide alone. This proved true in both *E. coli*. (ATCC 25922) and *S. aureus* (ATCC 25923). We thus conclude that the **Spd** delivery strategy described here may have a role to play in overcoming the limitations of bioactive functional peptides. Ultimately, this could lead to the development of more effective peptide-based diagnostic and therapeutic agents.

EXPERIMENTAL SECTION

Synthesis of DCM$_7$-*β*-CD.

To a stirred solution of per-*O*-acetylated 6-azido-6-deoxy-*β*-cyclodextrin (445.7 mg, 0.233 mmol) in CH_3CN (10 mL), were added, respectively, $Cu(SO_4)_2{\cdot}5H_2O$ (24.8 mg, 0.099 mmol), sodium ascorbate (76.6 mg, 0.387 mmol), and the requisite DCM-alkyne (678.7 mg, 1.641 mmol). The mixture was heated 30 min at 130 °C under microwave irradiation (6.3 bar, 30 mL reactor, 1000 rpm). The volatiles were then removed under vacuum. The resulting crude product was obtained without extraction and carefully purified in the dark by means of silica gel chromatography using EtOAc followed by a mixture EtOAc/EtOH (gradient 95/5, 9/1). This gave 78% of the desired compound (872 mg) as a dark red solid. R_f = 0.61 (EtOAc/EtOH, 95/5, v/v); $[\alpha]_D^{24}$ – 89(*c* 0.2, $CHCl_3$; mp = 212–220 °C; ^{1}H NMR (400 MHz, $CDCl_3$)δ = 1.36 (s, 63H, $CH_{3\ tBu}$), 2.03 (s, 21H, $CH_{3\ OAc}$), 2.08 (s, 21H, $CH_{3\ OAc}$), 2.98 (s, 21H, $CH_{3\ NMe}$), 3.45–3.60 (m, 21H, CH_2, H-4), 3.62–3.75 (m, 14H, CH_2), 4.44–4.59 (m, 21H, OCH_2, H-5), 4.67–4.82 (m, 14H, H-2, H-6), 4.88–5.02 (m, 7H, H-6'), 5.39 (t, *J* = 9.2 Hz, 7H, H-3), 5.51 (bs, 7H, H-1), 6.41 (d, *J* = 15.6 Hz, 7H, C*H*=), 6.47–6.49 (m, 14H, C*H*=), 6.65 (d, *J* = 8.7 Hz, 14H, H_{Ar}), 7.28 (d, *J* = 15.6 Hz, 7H, C*H*=), 7.37 (d, *J* = 8.7 Hz, 14H, H_{Ar}), 7.78 (s, 7H, $H_{triazole}$). ^{13}C NMR (100 MHz, $CDCl_3$) δ = 20.78, 20.80 ($CH_{3\ OAc}$); 28.14 ($CH_{3\ tBu}$), 36.64 ($C_{q\ tBu}$), 39.02 ($CH_{3\ NMe}$), 50.06 (C_6), 51.87 (CH_2), 57.49 (C_q), 64.61, 68.05 (CH_2); 69.75 (C_5), 69.88 (C_2), 70.45 (C_3), 76.70 (C_4), 96.46 (C_1), 102.33, 105.44, 111.89, 112.91 (*C*H); 115.75, 115.90, 122.40 (C_q); 125.58 ($CH_{triazole}$), 129.82, 138.25 (CH_{Ar}); 144.91, 150.74, 156.78, 160.20, 169.48, 170.47, 171.92 (C_q). ESI-HRMS *m*/*z* calcd for $C_{252}H_{282}N_{42}O_{56}$ $[M+2H]^{2+}$ 2397.5300, obsd 2397.5292; calcd for $C_{252}H_{283}N_{42}O_{56}$ $[M+3H]^{3+}$ 1598.6891, obsd 1598.6896; calcd for $C_{252}H_{284}N_{42}O_{56}$ $[M+4H]^{4+}$ 1199.2686, obsd 1199.2690; calcd for $C_{252}H_{285}N_{42}O_{56}$ $[M+5H]^{5+}$ 959.4157, obsd 959.4162; calcd for $C_{252}H_{286}N_{42}O_{56}$ $[M+6H]^{6+}$ 799.8482, obsd 799.8491.

Dose and Time-Dependent Fluorescence Imaging of Hep-G2 cells by Spd-1.

Hep-G2 cells were cultured in HG-DMEM containing 10% fetal bovine serum. For dose-dependent experiments, the cells were treated with 500 μM of palmitic acid (PA) for 24 h and then incubated with **Spd-1** for 30 min at indicated concentrations, followed by addition of the nuclear staining reagent Hoechst for 5 min. For time-dependent experiments, Hep-G2 cells were incubated with 500 μm PA for 0, 12, and 24 h. Then, **Spd-1** was added to cells and incubated for 30 min. The cells were washed with PBS three times, and images were taken using an Operetta high content imaging system (PerkinElmer). Fluorescence quantification was carried out by the Columbus image data analysis system (PerkinElmer). The mean fluorescence intensity of cell regions (A) and that of background (B) was calculated separately using the Columbus image data analysis system (PerkinElmer). Quantification was achieved by subtracting B from A. More than 500 cells were quantified in each pass. Excitation and emission channels for FITC are 460–490 and 500–550 nm, respectively. The excitation and emission channels for Hoechst is 360–400 and 410–480 nm, respectively.

Determination of Bacterial Viability in Vitro.

The plate counting method measuring the number of CFU was used to test the antibacterial effect of **P4** in the presence and absence of **DCM$_7$-β-CD**. *Escherichia coli* (*E. coli*, ATCC 25922), *Staphylococcus aureus* (*S. aureus*, ATCC 25923), the clinically isolated *Pseudomonas aeruginosa* (*P. aeruginosa*, 3887), and *Acinetobacter baumannii* (*A. baumannii*, AB-1617) were seeded at a density of 10^6 cells mL^{-1} in a 96-well plate, followed by incubation with **P4** (20 μM), **DCM$_7$-β-CD** (20 μM), and **Spd-4** (**P4**/**DCM$_7$-β-CD**= 20 μM/20 μM). The mixture was incubated at 37 °C for 4 h, and then the mixture was diluted 10^1, 10^2, 10^3, 10^4, 10^5, and 10^6 times using sterile water. Subsequently, a 5 μL aliquot of the diluent with different concentrations was spread three times onto a plate according to plate-spreading method. Each plate was finally incubated at 37 °C for 18 h, and then the average CFUs of the diluent were counted and calculated. Photographs were also taken. For the bacterial viability determination, the average CFUs of the control group were defined as 100%, and those of other groups were calculated accordingly.

Supplementary Material

Refer to Web version on PubMed Central for supplementary material.

ACKNOWLEDGMENTS

The authors thank the National Natural Science Foundation of China (Nos. 21788102, 91853201, 21722801, 81673489, and 31871414), the Shanghai Municipal Science and Technology Major Project (No. 2018SHZDZX03), the International Cooperation Program of Shanghai Science and Technology Committee (No. 17520750100) and the Fundamental Research Funds for the Central Universities (222201717003) for financial support. The work in France was supported by the COST Action Functional Glyconanomaterials for the Development of Diagnostics and Targeted Therapeutic Probes (CA18132). The work in Austin was supported by the National Institutes of Health (GM RO1 103790 to J.L.S.) and the Robert A. Welch Foundation (F-0018).

REFERENCES

(1). Cunningham-Bryant D; Dieter EM; Foight GW; Rose JC; Loutey DE; Maly DJ A Chemically Disrupted Proximity System for Controlling Dynamic Cellular Processes. J. Am. Chem. Soc 2019, 141, 3352–3355. [PubMed: 30735038]

(2). Liu W; Beck BH; Vaidya KS; Nash KT; Feeley KP; Ballinger SW; Pounds KM; Denning WL; Diers AR; Landar A; Iwakuma T; Welch DR Metastasis Suppressor KISS1 Seems to Reverse the Warburg Effect by Enhancing Mitochondrial Biogenesis. Cancer Res 2014, 74, 954–963. [PubMed: 24351292]

(3). Krishnan RS; Satheesan R; Puthumadathil N; Kumar KS; Jayasree P; Mahendran KR Autonomously Assembled Synthetic Transmembrane Peptide Pore. J. Am. Chem. Soc 2019, 141, 2949–2959. [PubMed: 30702873]

(4). He WX; Wang S; Yan J; Qu Y; Jin L; Sui F; Li Y; You W; Yang G; Yang Q; Ji M; Shao Y; Ma PX; Lu W; Hou P Self-Assembly of Therapeutic Peptide into Stimuli-Responsive Clustered Nanohybrids for Cancer-Targeted Therapy. Adv. Funct. Mater 2019, 29, 1807736–1807751. [PubMed: 32982625]

(5). Anderson RJ; Tang CW; Daniels NJ; Compton BJ; Hayman CM; Johnston KA; Knight DA; Gasser O; Poyntz HC; Ferguson PM; Larsen DS; Ronchese F; Painter GF; Hermans IF A self-adjuvanting vaccine induces cytotoxic T lymphocytes that suppress allergy. Nat. Chem. Biol 2014, 10, 943–949. [PubMed: 25282504]

(6). Godwin HA; Berg JM A Fluorescent Zinc Probe Based on Metal-Induced Peptide Folding. J. Am. Chem. Soc 1996, 118, 6514–6515.

(7). Vazquez ME; Nitz M; Stehn J; Yaffe MB; Imperiali B Fluorescent caged phosphoserine peptides as probes to investigate phosphorylation-dependent protein associations. J. Am. Chem. Soc 2003, 125, 10150–10151. [PubMed: 12926919]

(8). Lau JL; Dunn MK Therapeutic peptides: Historical perspectives, current development trends, and future directions. Bioorg. Med. Chem 2018, 26, 2700–2707. [PubMed: 28720325]

(9). Sun XL; Li Y; Liu T; Li Z; Zhang X; Chen X Peptide-based imaging agents for cancer detection. Adv. Drug Delivery Rev 2017, 110, 38–51.

(10). Shi HB; Kwok RT; Liu JZ; Xing BG; Tang BZ; Liu B Real-time monitoring of cell apoptosis and drug screening using fluorescent light-up probe with aggregation-induced emission characteristics. J. Am. Chem. Soc 2012, 134, 17972–17981. [PubMed: 23043485]

(11). Vinogradov AA; Yin Y; Suga H Macrocyclic Peptides as Drug Candidates: Recent Progress and Remaining Challenges. J. Am. Chem. Soc 2019, 141, 4167–4181. [PubMed: 30768253]

(12). Ma Y-H; Dou W-T; Pan Y-F; Dong L-W; Tan Y-X; He X-P; Tian H; Wang H-Y 2D Materials: Fluorogenic 2D Peptidosheet Unravels CD47 as a Potential Biomarker for Profiling Hepatocellular Carcinoma and Cholangiocarcinoma Tissues. Adv. Mater 2017, 29, 1604253–1604259.

(13). Chu TT; Gao N; Li QQ; Chen PG; Yang XF; Chen YX; Zhao YF; Li YM Specific Knockdown of Endogenous Tau Protein by Peptide-Directed Ubiquitin-Proteasome Degradation. Cell Chem. Biol 2016, 23, 453–461.

(14). Hyun S; Choi Y; Lee HN; Lee C; Oh D; Lee DK; Lee C; Lee Y; Yu J Construction of histidine-containing hydrocarbon stapled cell penetrating peptides for in vitro and in vivo delivery of siRNAs. Chem. Sci 2018, 9, 3820–3827. [PubMed: 29780514]

(15). Guidotti G; Brambilla L; Rossi D Cell-Penetrating Peptides: From Basic Research to Clinics. Trends Pharmacol. Sci 2017, 38, 406–424. [PubMed: 28209404]

(16). Kumar M; Tegge W; Wangoo N; Jain R; Sharma RK Insights into cell penetrating peptide conjugated gold nanoparticles for internalization into bacterial cells. Biophys. Chem 2018, 237, 38–46. [PubMed: 29656216]

(17). Han HH; Qiu YJ; Shi YY; Wen W; He X-P; Dong LW; Tan YX; Long YT; Tian H; Wang HY Glypican-3-targeted precision diagnosis of hepatocellular carcinoma on clinical sections with a supramolecular 2D imaging probe. Theranostics 2018, 8, 3268–3274. [PubMed: 29930728]

(18). Li QR; Jiao JB; Li LL; He X-P; Zang Y; James TD; Chen GR; Guo L; Li J Graphene oxide-enhanced cytoskeleton imaging and mitosis tracking. Chem. Commun 2017, 53, 3373–3376.

(19). Lock LL; Reyes CD; Zhang P; Cui H Tuning Cellular Uptake of Molecular Probes by Rational Design of Their Assembly into Supramolecular Nanoprobes. J. Am. Chem. Soc 2016, 138, 3533–3540. [PubMed: 26890853]

(20). Poorghorban M; Karoyo AH; Grochulski P; Verrall RE; Wilson LD; Badea IA ^{1}H NMR Study of Host/Guest Supramolecular Complexes of a Curcumin Analogue with beta-Cyclodextrin and a beta-Cyclodextrin-Conjugated Gemini Surfactant. Mol. Pharmaceutics 2015, 12, 2993–3006.

(21). Jiang Q; Zhang Y; Zhuo R; Jiang X A light and reduction dual sensitive supramolecular self-assembly gene delivery system based on poly(cyclodextrin) and disulfide-containing azobenzene-terminated branched polycations. J. Mater. Chem. B 2016, 4, 7731–7740. [PubMed: 32263830]

(22). Xiong H; Zhou D; Zheng X; Qi Y; Wang Y; Jing X; Huang Y Stable amphiphilic supramolecular self-assembly based on cyclodextrin and carborane for the efficient photodynamic therapy. Chem. Commun 2017, 53, 3422–3425.

(23). Hu Qi. Da.; Tang GP; Chu PK Cyclodextrin-Based Host - Guest Supramolecular Nanoparticles for Delivery: From Design to Applications. Acc. Chem. Res 2014, 47, 2017–2025. [PubMed: 24873201]

(24). Lai WF; Rogach AL; Wong WT Chemistry and engineering of cyclodextrins for molecular imaging. Chem. Soc. Rev 2017, 46, 6379–6419. [PubMed: 28930330]

(25). Martinez A; Ortiz Mellet C; Garcia Fernandez JM Cyclodextrin-Based Multivalent Glycodisplays: Covalent and Supramolecular Conjugates to Assess Carbohydrate -Protein Interactions. Chem. Soc. Rev 2013, 42, 4746–4773. [PubMed: 23340678]

(26). Segredo-Morales E; Martin-Pastor M; Salas A; Evora C; Concheiro A; Alvarez-Lorenzo C; Delgado A Mobility of Water and Polymer Species and Rheological Properties of Supramolecular Polypseudorotaxane Gels Suitable for Bone Regeneration. Bioconjugate Chem 2018, 29, 503–516.

(27). (a)He X-P; Li R-H; Maisonneuve S; Ruan Y; Chen G-R; Xie J Fluorogenic supramolecular complex formed between pyrenyl-β-cyclodextrin and glyco-rhodamine for the selective detection of lectins. Chem. Commun 2014, 50, 14141–14144.(b)De Schutter C; Roy V; Favetta P; Pavageau C; Maisonneuve S; Bogliotti N; Xie J; Agrofoglio LA Synthesis and caracterization of various 5′-dye-labeled ribonucleosides. Org. Biomol. Chem 2018, 16, 6552–6563. [PubMed: 30168548] (c)Wang H; Liu Y; Xu C; Wang X; Chen GR; James TD; Zang Y; Li J; Ma X; He X-P Supramolecular glyco-poly-cyclodextrin functionalized thin-layer manganese dioxide for targeted stimulus-responsive bioimaging. Chem. Commun 2018, 54, 4037–4040.

(28). Maisonneuve S; Fang Q; Xie J Benzothiadiazoyl-triazoylcyclodextrin: a selective fluoroionophore for Ni(II). Tetrahedron 2008, 64, 8716–8720.

(29). David O; Maisonneuve S; Xie J Generation of new fluorophore by Click chemistry: synthesis and properties of β-cyclodextrin substituted by 2-pyridyl triazole. Tetrahedron Lett 2007, 48, 6527–6530.

(30). Vickers CJ; González-Paéz GE; Wolan DW Selective detection and inhibition of active caspase-3 in cells with optimized peptides. J. Am. Chem. Soc 2013, 135, 12869–12876. [PubMed: 23915420]

(31). Cao B; Mao C Identification of microtubule-binding domains on microtubule-associated proteins by major coat phage display technique. Biomacromolecules 2009, 10, 555–564. [PubMed: 19186939]

(32). Liu P; Li B; Zhan C; Fang Z; Wu S A Two-Photon-Activated Prodrug for Therapy and Drug Release Monitoring. J. Mater. Chem. B 2017, 5, 7538–7546. [PubMed: 32264229]

(33). Qin Y; Shi J; Gong X; Tian Z; Ping Z; Lu J A Luminescent Inorganic/Organic Composite Ultrathin Film Based on a 2D Cascade FRET Process and Its Potential VOC Selective Sensing Properties. Adv. Funct. Mater 2016, 26, 6752–6759.

(34). Lu KY; Lin CW; Hsu CH; Ho YC; Chuang EY; Sung HW; Mi FL FRET-Based Dual-Emission and pH-Responsive Nanocarriers for Enhanced Delivery of Protein Across Intestinal Epithelial Cell Barrier. ACS Appl. Mater. Interfaces 2014, 6, 18275–18289. [PubMed: 25260022]

(35). Vickers CJ; González-Paéz GE; Wolan DW Discovery of a highly selective caspase-3 substrate for imaging live cells. ACS Chem. Biol 2014, 9, 2199–2203. [PubMed: 25133295]

(36). Ricchi M; Odoardi MR; Carulli L; Anzivino C; Ballestri S; Pinetti A; Fantoni LI; Marra F; Bertolotti M; Banni S; Lonardo A; Carulli N; Loria P Differential effect of oleic and palmitic acid on lipid accumulation and apoptosis in cultured hepatocytes. J. Gastroenterol. Hepatol 2009, 24 (5), 830–840. [PubMed: 19207680]

(37). Chinen T; Liu P; Shioda S; Pagel J; Cerikan B; Lin T-C; Gruss O; Hayashi Y; Takeno H; Shima T; Okada Y; Hayakawa I; Hayashi Y; Kigoshi H; Usui T; Schiebel E The γ-tubulin-specific inhibitor gatastatin reveals temporal requirements of microtubule nucleation during the cell cycle. Nat. Commun 2015, 6, 8722–8733. [PubMed: 26503935]

(38). Hofer U The cost of antimicrobial resistance. Nat. Rev. Microbiol 2019, 17, 3–11. [PubMed: 30467331]

(39). Gao X; Chen Y; Chen Z; Xue Z; Jia Y; Guo Q; Ma Q; Zhang M; Chen H Identification and antimicrobial activity evaluation of three peptides from laba garlic and the related mechanisms. Food Funct 2019, 10, 4486–4496. [PubMed: 31241636]

(40). Kohanski MA; Dwyer DJ; Collins JJ How antibiotics kill bacteria: from targets to networks. Nat. Rev. Microbiol 2010, 8, 423–435. [PubMed: 20440275]

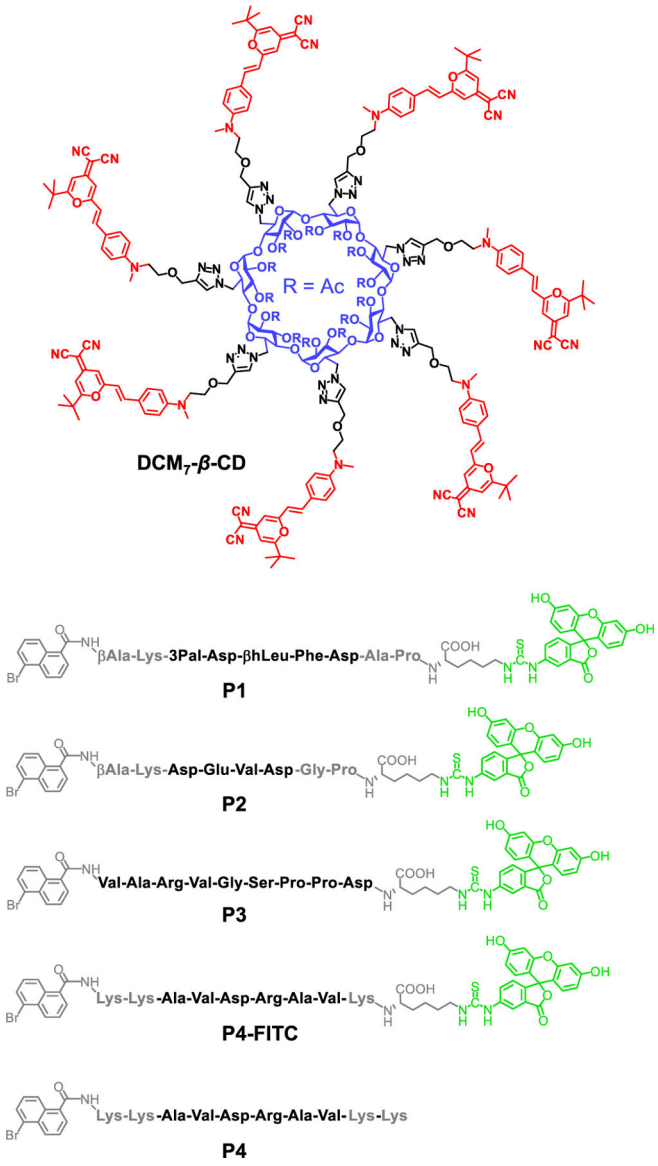

Figure 1.

Structure of the hepta-dicyanomethylene-4*H*-pyran appended *β*-cyclodextrin (**DCM$_7$-*β*-CD**) and the fluorescent (**P1–P3**) and antimicrobial (**P4**) peptide probes considered in this study.

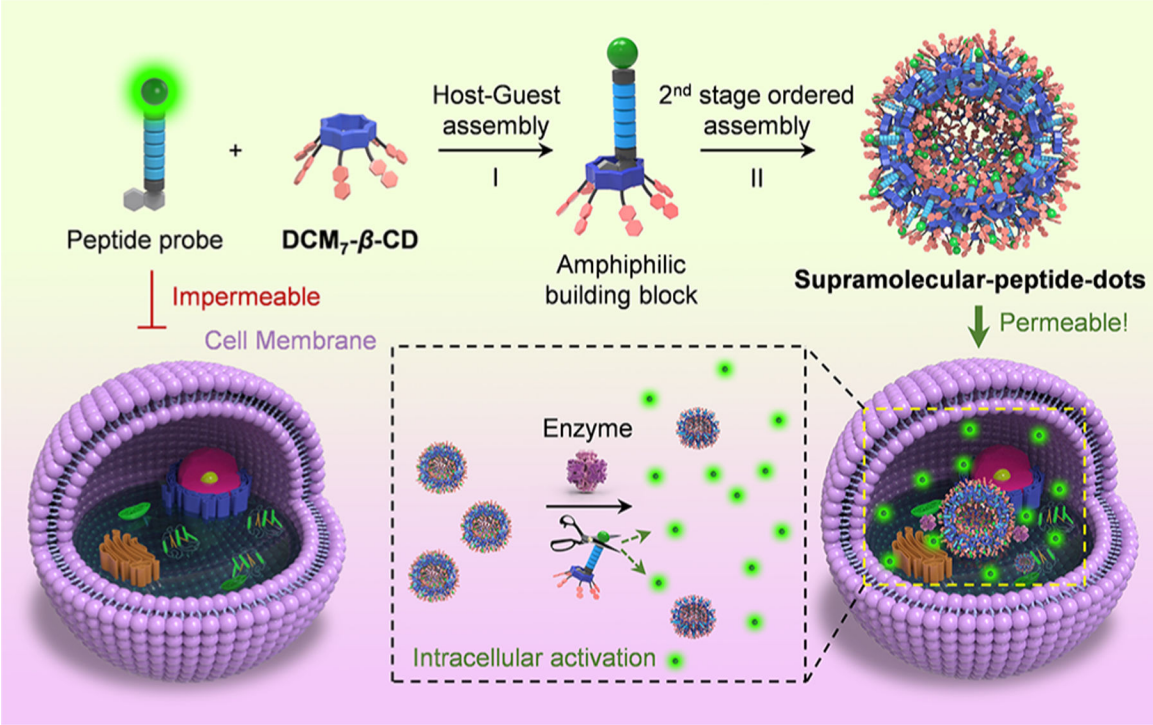

Figure 2.

Schematic illustration of the sequential host–guest and second-stage ordered self-assembly between probes **P1–P3** and **DCM$_7$-*β*-CD** to give so-called supramolecular-peptide-dots (**Spds**) with enhanced cellular uptake and functional imaging features. The fluorescent green dots are used to designate individual FITC moieties.

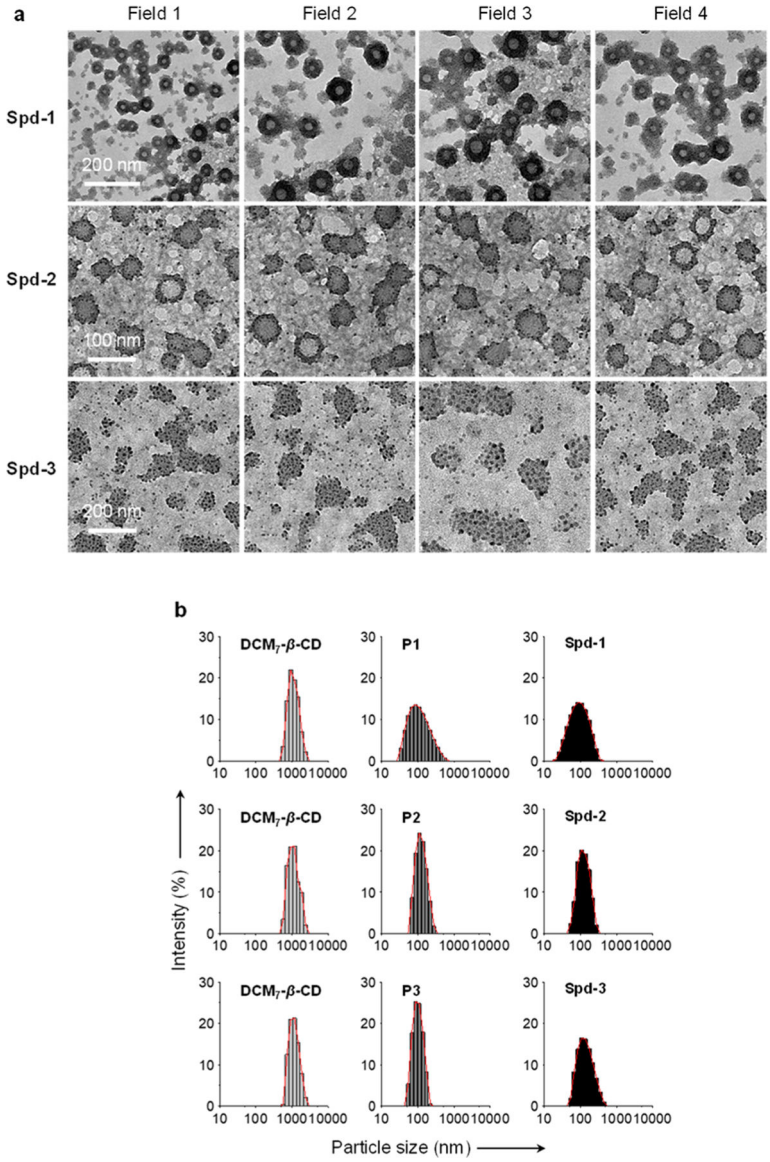

Figure 3.

(a) High-resolution transmission electron microscopic images of **Spd-1** (**P1**/DCM$_7$-β-CD = 4 μM/4 μM), **Spd-2** (**P2**/DCM$_7$-β-CD = 4 μM/4 μM), and **Spd-3** (**P3**/DCM$_7$-β-CD = 4 μM/4 μM) recorded on a JEM-2100 TEM system. (b) Dynamic light scattering analyses of DCM$_7$-β-CD (4 μM), **P1** (4 μM), **P2** (4 μM), **P3** (4 μM), **Spd-1** (**P1**/DCM$_7$-β-CD = 4 μM/4 μM), **Spd-2** (**P2**/DCM$_7$-β-CD = 4 μM/4 μM), and **Spd-3** (**P3**/DCM$_7$-β-CD = 4 μM/4 μM).

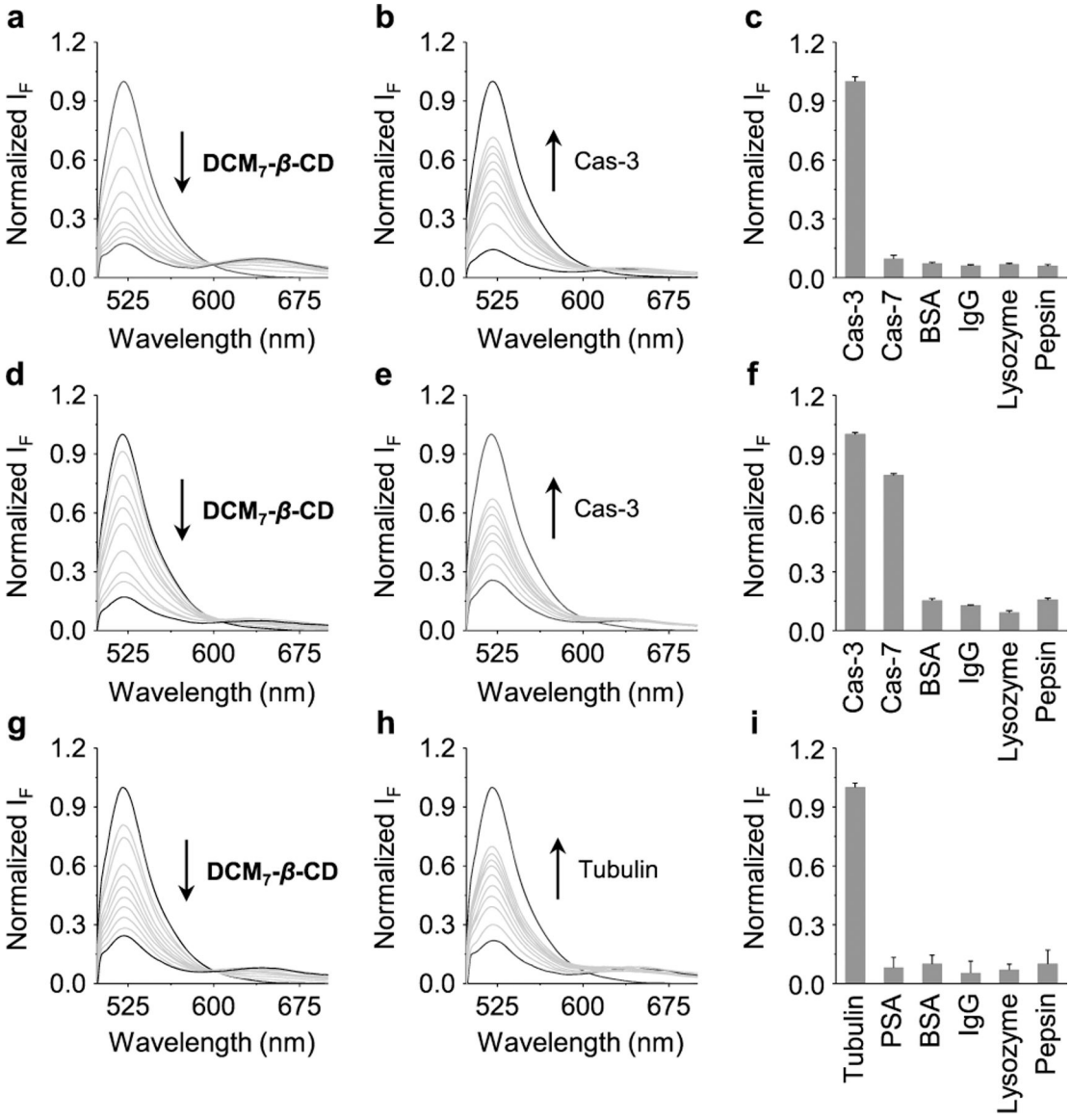

Figure 4.

(a) Fluorescence spectra of **P1** (0.17 μM) recorded in the presence of increasing concentrations DCM$_7$-β-CD (0–7.3 μM). (b) Fluorescence spectra of **Spd-1** (**P1**/DCM$_7$-β-CD = 0.17 μM/7.3 μM) recorded in the presence of increasing caspase-3, (Cas-3; 0–46 nM). (c) Normalized fluorescence intensity of **Spd-1** (**P1**/DCM$_7$-β-CD = 0.167 μM/7.3 μM) recorded in the presence of Cas-3 (46 nM) or other proteins (46 nM) (Cas-7 = caspase-7; BSA= bovine serum albumin; IgG = immunoglobulin G). (d) Fluorescence spectra of **P2** (0.25 μM) recorded in the presence of increasing DCM$_7$-β-CD (0–6 μM). (e) Fluorescence spectra of **Spd-2** (**P2**/DCM$_7$-β-CD = 0.25 μM/6 μM) recorded in the presence of increasing Cas-3 (0–46 nM). (e) Fluorescence spectra of **Spd-2** (**P2**/DCM$_7$-β-CD = 0.25 μM/6 μM) recorded in the presence of increasing Cas-3 (0–46 nM). (f) Normalized fluorescence intensity of **Spd-2** (**P2**/DCM$_7$-β-CD = 0.25 μM/6 μM) recorded in the presence of Cas-3 (46 nM) and other proteins (46 nM). (g) Fluorescence spectra of **P3** (0.25 μM) recorded in the

presence of increasing DCM_7-β-CD (0–5 μM). (h) Fluorescence spectra of **Spd-3** (**P3**/DCM_7-β-CD = 0.25 μM/5 μM) recorded in the presence of increasing tubulin (0–36 nM). (i) Normalized fluorescence spectra of **Spd-3** (**P3**/DCM_7-β-CD, 0.25 μM/5 μM) recorded in the presence of tubulin (36 nM) and other proteins (36 nM) (PSA = *Pisum sativum* agglutinin). All fluorescence measurements were carried out in phosphate buffered saline solution (0.1 M, pH 7.4) with an excitation wavelength of 470 nm.

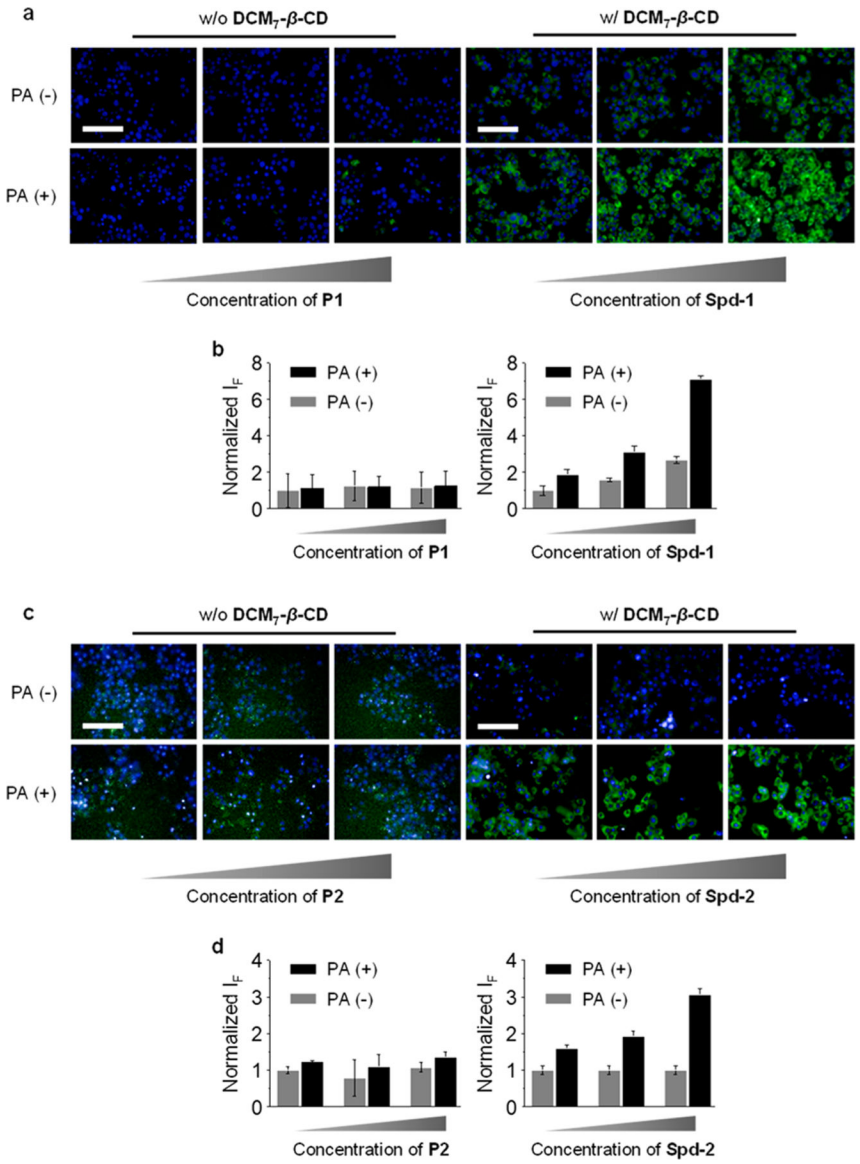

Figure 5.

Dose-dependent fluorescence imaging (a) and quantification (b) of Hep-G2 cells (preincubated with 500 μM of palmitic acid (PA)) treated with **P1** (0.2 μM, 0.5 μM, 1 μM) or **Spd-1** (**P1**/DCM$_7$-β-CD = 0.2/4 μM, 0.5/5 μM, 1/8 μM). Dose-dependent fluorescence imaging (c) and quantification (d) of Hep-G2 cells (preincubated with 500 μM of palmitic acid (PA)) treated with **P2** (0.25 μM, 0.5 μM, 1 μM) or **Spd-2** (**P2**/DCM$_7$-β-CD = 0.25/4 μM, 0.5/5 μM, 1/8 μM). Excitation and emission channels for FITC are 460–490 and 500–550 nm, respectively. Cell nuclei were stained by Hoechst (excitation and emission channels are 360–400 and 410–480 nm, respectively). Scale bar = 100 μm (applicable to all images in panels and c).

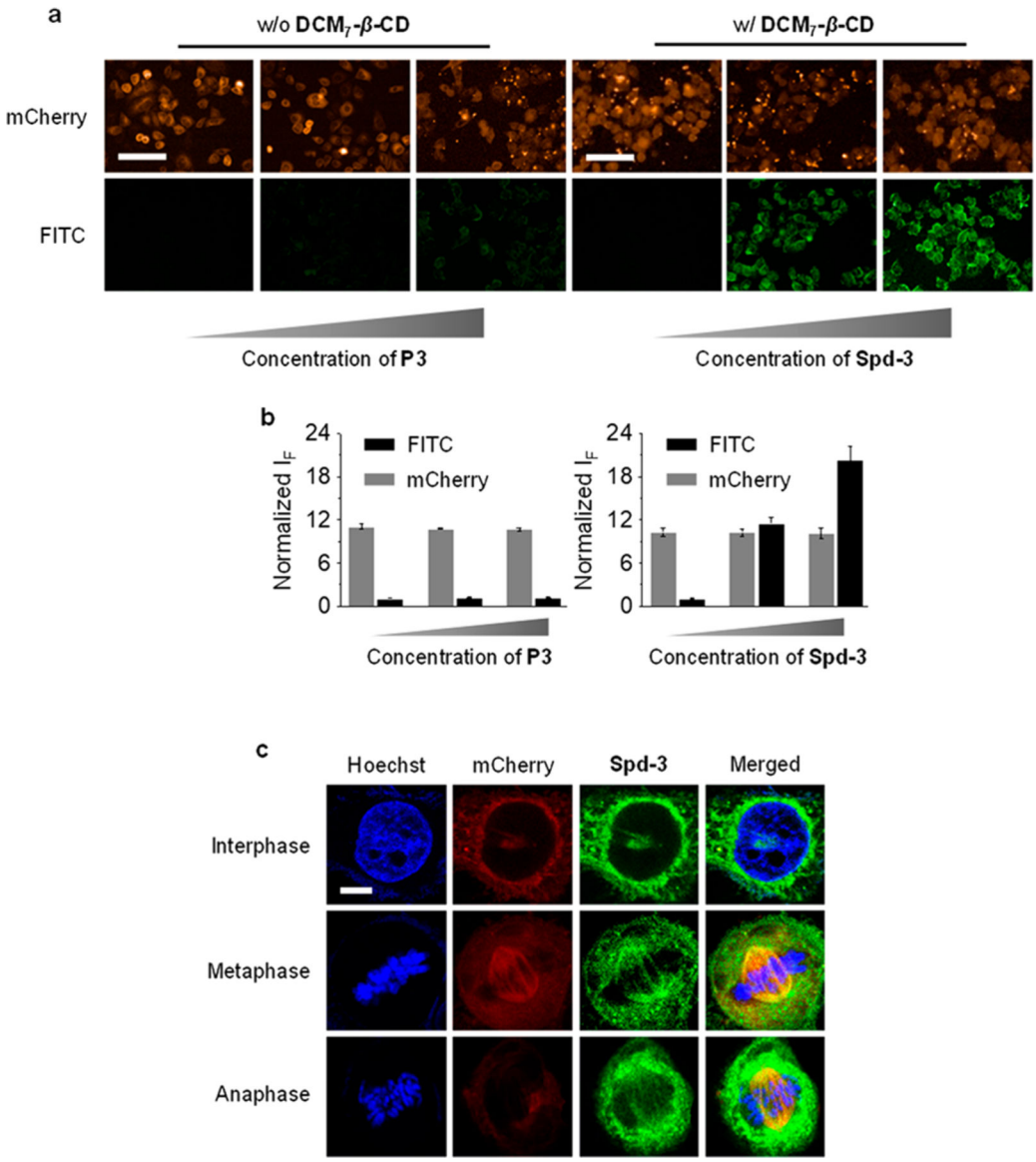

Figure 6.

Dose-dependent fluorescence imaging (a) and quantification (b) of HeLa cells treated with **P3** (0.25, 0.5, and 1 μM) or **Spd-3** (**P3**/DCM$_7$-β-CD = 0.25/4 μM, 0.5/5 μM, 1/8 μM). HeLa cells using stably expressed mCherry-α-tubulin for cell mitosis imaging. Excitation and emission channels for FITC are 460–490 and 500–550 nm, respectively. Excitation and emission channels for mCherry are 560–580 and 580–650 nm, respectively. Cell nuclei were stained by Hoechst (excitation and emission channels are 360–400 and 410–480 nm, respectively). (c) Imaging of mitosis of HeLa cells by confocal microscopy. Excitation channels for DNA (stained by Hoechst), FITC, and mCherry are 405, 488, and 552 nm, respectively. Emission channels for DNA, FITC, and mCherry are 430–480, 490–540, and 570–640 nm, respectively. Scale bar = 100 μm (applicable to all images in Figure 6a); scale bar = 20 μm (applicable to all images in Figure 6e).

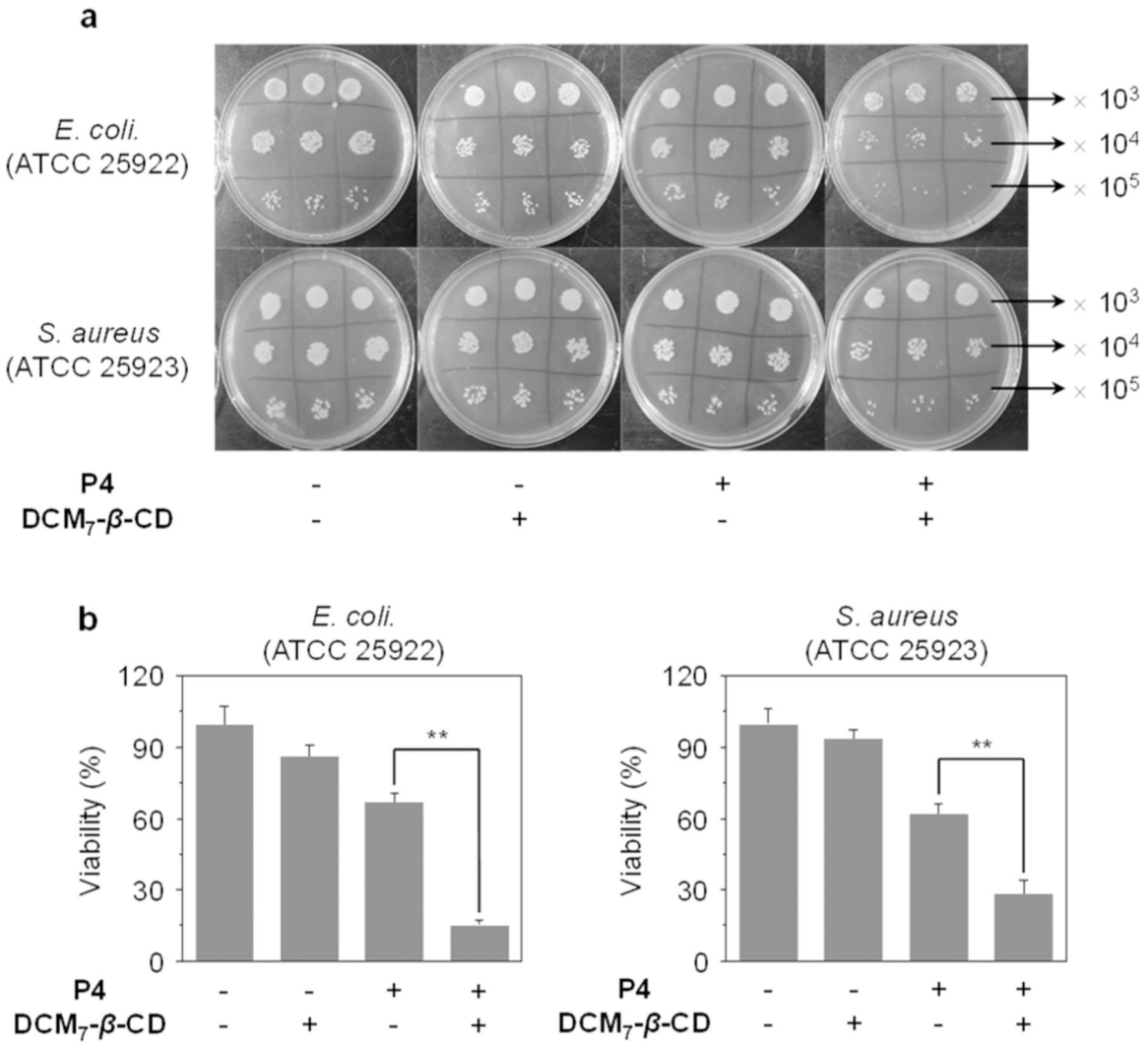

Figure 7.

(a) Bacterial cultures of *Escherichia coli* (*E. coli*, ATCC 25922) and *Staphylococcus aureus* (*S. aureus* ATCC 25923) without and with treatment with **P4**, **DCM$_7$-β-CD**, and **Spd-4**. (b) Relative bacterial viability of *Escherichia coli* (*E. coli*, ATCC 25922) and *Staphylococcus aureus* (*S. aureus* ATCC 25923) without and with treatment with **P4**, **DCM$_7$-β-CD**, and **Spd-4**. The concentrations of **P4**, **DCM$_7$-β-CD**, and **Spd-4** (**P4**/**DCM$_7$-β-CD**) were 20, 20, and 20 μM/20 μM, respectively. $^{**}P < 0.01$. Bacteria were $\times 10^3$, $\times 10^4$ and $\times 10^5$ diluted; the viability in Figure 7b is the ratio of the counted bacterium number ($\times 10^5$ diluted) in each group relative to that of the control group (bacteria alone).